J. Mech. Phys. Solids 181 (2023) 105439

Contents lists available at ScienceDirect

Journal of the Mechanics and Physics of Solids

journal homepage: www.elsevier.com/locate/jmps

Dissipation mechanisms of crack-parallel stress effects on fracture process zone in concrete

Yuhui Lyu [a], Madura Pathirage [b,1], Hoang T. Nguyen [c,1], Zdeněk P. Bažant [a,*], Gianluca Cusatis [a]

[a] Department of Civil and Environmental Engineering, Northwestern University, Evanston, IL 60208, USA
[b] Gerald May Department of Civil, Construction and Environmental Engineering, University of New Mexico, Albuquerque, NM 87131, USA
[c] School of Engineering, Brown University, Providence, RI 02912, USA

ARTICLE INFO

Keywords:
Gap test
Fracture parameters
Fracture mechanism
Fracture energy
Energy dissipation
Lattice discrete modeling
Material particle models
Frictional slip
Numerical simulation of fracture

ABSTRACT

The effect of crack-parallel stresses on the fracture properties of quasi-brittle materials has recently received significant attention in the fracture mechanics community. A new experiment, the so-called gap test, was developed to reveal this effect. While the finite element crack band model (CBM) with the physically realistic Microplane damage model M7 was quite successful in capturing the damage and fracture during the gap test, some questions remain, particularly the near doubling of the fracture energy at moderate crack parallel compression, which was underestimated by about 30%. Presented here is an in-depth meso-mechanical investigation of energy dissipation mechanisms in the Fracture Process Zone (FPZ) during the gap test of concrete, an archetypal quasi-brittle material. The Lattice Discrete Particle Model (LDPM) is here used to simulate the quasi-brittle material at the mesoscale, which is the length scale of major heterogeneities. The LDPM can capture accurately the frictional sliding, mixed-mode fracture, and FPZ development. The model parameters characterizing the given mix design are first calibrated by standard laboratory tests, namely the hydrostatic, unconfined compression, and four-point bending (4PB) tests. The experimental data used characteristic of the given mix design are calibrated by the Brazilian split-cylinder tests and by gap tests of different sizes with and without crack-parallel stresses. The results show that crack-parallel stresses affect not only the length but also the width of the FPZ. It is found that the energy dissipation portion under crack-parallel compression is significantly larger than it is under tension, which is caused by micro-scale frictional shear slips, as intuitively suggested in previous work. For large compressive stresses, the failure mode changes to inclined compression-shear bands consisting of axial splitting microcracks. Several complications experienced in the numerical modeling of gap tests are also discussed, and the solutions provided.

1. Introduction

In fracture mechanics of quasi-brittle materials, the effect of crack-parallel stresses has rarely been discussed and, prior to 2020, not even tested and quantitatively analyzed. Nevertheless, since the later 1960s, it has been clear that stress triaxiality in the fracture process zone (FPZ) ought to play some role. Clough (1962) and Clough and Wilson (1962) introduced the interelement line cracks

* Correspondence to: Northwestern University, 2145 Sheridan Rd, Tech Building Room A135, Evanston, IL 60208-3109, USA.
E-mail address: z-bazant@northwestern.edu (Z.P. Bažant).
[1] Formerly at Northwestern University.

https://doi.org/10.1016/j.jmps.2023.105439
Received 6 July 2023; Received in revised form 31 August 2023; Accepted 9 September 2023
Available online 20 September 2023

in his epoch-making 1962 analysis of cracks observed in Norfolk Dam (using finite elements of a continuum which he was the first to derive in 1960 Clough (1960), variationally). Ngo and Scordelis in 1967 (Ngo and Scordelis, 1967) used the interelement cracks in their analysis of cracking in beams. The fracture mechanics concepts were not used in these early studies.

Rashid, in 1968 (Rashid, 1968), analyzing a concrete nuclear reactor vessel, introduced into FE analysis the smeared fracturing characterized by a triaxial constitutive law with a sudden stress drop, while Scanlon introduced in 1971 the gradual postpeak softening (Scanlon, 1971). Most nuclear, dam and other structures designed by FE in the 1960s and 1970s are still in service.

The smeared cracking concept inevitably ignited debate about the importance of stress triaxiality in the FPZ at the fracture front. In 1976 it was shown (Bažant, 1976) that a constitutive law with postpeak softening requires a finite material characteristic length l_0 as a strain localization limiter in the sense of smallest admissible constant strain finite element, i.e., a nonlocal continuum concept. In 1979, the blunt crack model with sudden stress drop in the FPZ (Bažant and Cedolin, 1979) and in 1983 (Bažant and Oh, 1983) the crack band model with progressive softening eliminated the spurious dependence on the FE size and made the triaxial smeared fracture model objective. Many other studies also addressed these problems, e.g., Huynh et al. (2019), Pijaudier-Cabot et al. (2022), Bazant and Planas (2019), Di Luzio et al. (2004), Barenblatt (1959) and Hillerborg et al. (1976).

The stress triaxiality in this smeared crack band invited the question of whether the crack-parallel normal stress may play some role. An attempt to check it experimentally was made in 1995 in Vienna by Tschegg et al. (1995). It showed that some effect existed, but the test was difficult to evaluate unambiguously because the crack parallel stress was varying during fracture growth, the compression stress field was nonuniform, with maxima farther away from the crack tip, and the setup was statically indeterminate, requiring an assumption of a realistic constitutive law and data fitting via FE simulations. Besides, a sophisticated experimental setup was needed. So, no quantitative conclusion was drawn. These obstacles were overcome by the emergence in 2020 of the gap test (Nguyen et al., 2020b,a; Brockmann and Salviato, 2022; Bažant et al., 2022b,a).

Why has the problem of crack-parallel stress remained dormant for such a long time? Doubtless for two reasons: (1) All the standard fracture specimens have a negligible crack parallel stress, so nothing can be detected, and (2) A lack of interest due to the fact that line crack models, such as Griffith's (LEFM) and cohesive crack model (CCM) (Barenblatt, 1959) (renamed by Hillerborg et al., 1976; Hillerborg, 1983 as the fictitious crack model), cannot capture it. Indeed, if the crack is really a line (or a plane in 3D), the crack parallel stress could have no effect on propagation. But a crack is never a line or a plane. This is clear for concrete. But even in polycrystalline metals, the crack front cannot be narrower than the size of the crystal, about 1 micrometer, and it does matter (Nguyen et al., 2021; Bažant et al., 2022c). In atomistically perfect cracks, as in graphene, the positions of the atoms on the side of the crack must be disturbed (or else the surface energy could not exist), and this must again cause sensitivity to crack-parallel stresses.

The gap test (Nguyen et al., 2020b,a; Brockmann and Salviato, 2022; Bažant et al., 2022b,a) recently emerged to provide new insights on the effect of crack-parallel stresses. It showed that crack-parallel stresses substantially affect the fracture properties of quasi-brittle materials.

It became clear that any change in the FPZ size, either FPZ width or length or both, leads to a specific change in fracture properties. Therefore, understanding how the size of the FPZ changes and how the energy is dissipated within the FPZ corresponding to different crack-parallel stress levels is essential to clarify the difference in fracture properties caused by crack-parallel stresses. However, it is challenging for experimental techniques to characterize the FPZ directly. Hence, state-of-the-art numerical models must be employed to study the complex interacting microscopic processes and their relation to macroscopic behavior when crack-parallel stresses exist.

A few FE continuum models can, to various extent, capture the changes in the fracture properties due to changes in the FPZ. The crack band model (CBM) (Bažant and Oh, 1983) underestimates the crack-parallel stress effect by only about 30%, which is due to fixed crack front width. The smeared crack model (SCM) (Jirásek, 2011) is another example. These two models with a tensorial softening damage constitutive law can capture the tensile microcracking in the FPZ and the effect of the lateral expansion of the FPZ caused by crack-parallel stresses (Bažant, 2002b; Ožbolt, 1996). When performing modeling, the classical CBM (Bažant and Oh, 1983) requires either a random mesh or adaptive mesh procedures, to remove mesh orientation bias. This is, however, avoided by the 2023 smooth crack band model (sCBM) (Zhang and Bažant, 2023) in which a limitation of maximum possible second gradient (or curvature) of the displacement vector field is used to resolve the distribution of damage across the material characteristic length and across the crack band, and simulate width changes of the crack front. The SCM has issues related to mesh sensitivity, which can be prohibitive from a computational cost point of view.

To overcome these challenges, the Lattice Discrete Particle Model (LDPM), which accounts for material heterogeneity at the length scale of coarse aggregate pieces, is here preferred for demonstrating and explaining the effects of crack-parallel stresses on the fracture behavior of quasi-brittle materials. The LDPM can simulate the mesoscale response of concrete, including cohesive fracturing, strain softening in tension, strain hardening in compression, material compaction due to pore collapse, and frictional slip (Cusatis et al., 2011b,a).

This study uses the LDPM in conjunction with the experimental data on gap test (Nguyen et al., 2020a). The LDPM material parameters were first calibrated using experimental data from the hydrostatic tests, uniaxial unconfined compression tests, and fracture tests. The hydrostatic tests, which are specifically required when considering crack-parallel stresses, are not routinely performed. However, the present experimentals (Nguyen et al., 2020a) did not include this test. Therefore, additional experimental data (Green and Swanson, 1973), obtained from the hydrostatic tests for similar concrete mix design, elastic modulus and Poisson's ratio, were used to identify parameters relevant to the volumetric compression behavior. After careful parameter identification, LDPM was utilized to predict the size-effect tests under different crack-parallel stress levels and Brazilian tests. Finally, the fracture propagation, fracture parameters, FPZ evolution, and distribution of energy dissipation due to damage under different crack-parallel stresses were investigated.

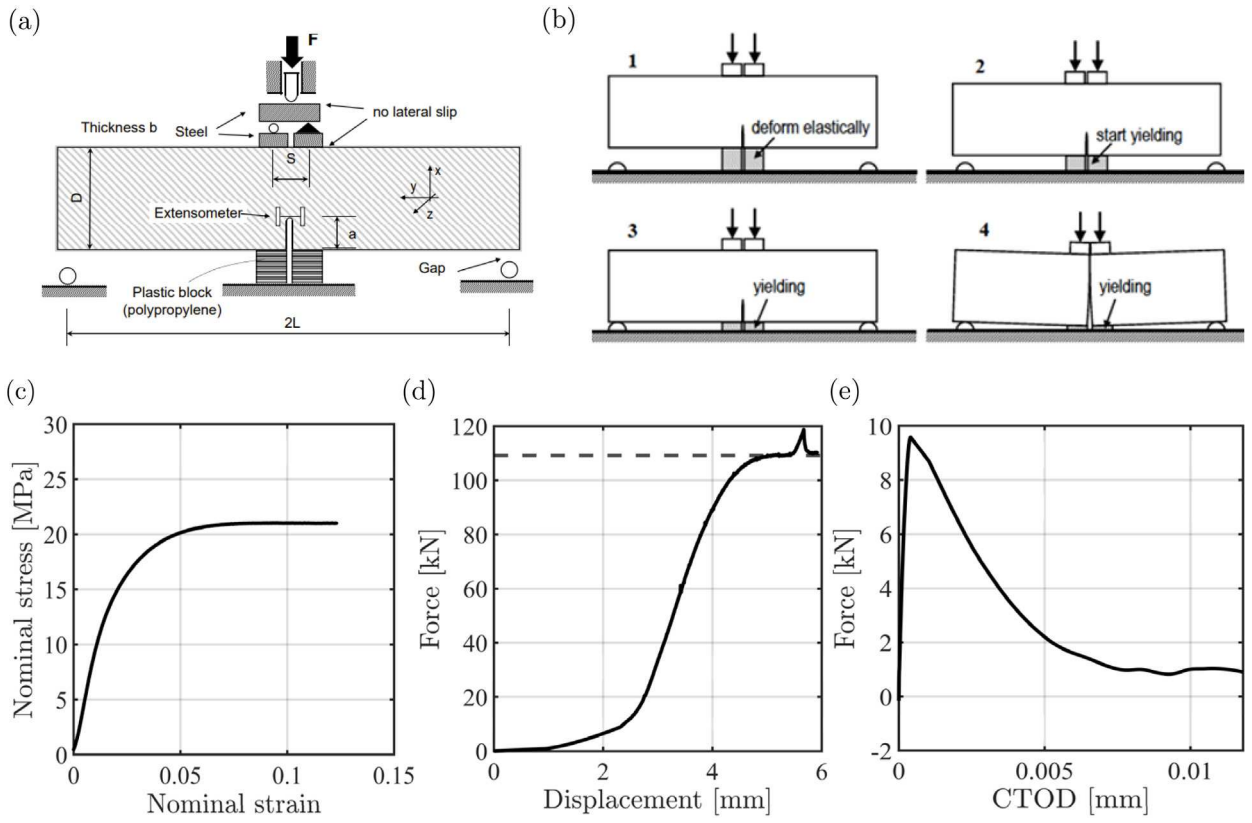

Fig. 1. (a) The experimental setup of the gap test; (b) Experimental procedures; (c) Stress–strain behavior of the plastic pad; (d) A representative load–displacement curve for the gap test; (e) The extracted load-CTOD curve;.

2. Background

2.1. Gap test

As stated above, although suspicions of crack-parallel compression effects on the fracture behavior of quasi-brittle materials have existed since the work of Tschegg and coworkers (Tschegg et al., 1995), this phenomenon remained obscure due to the difficulty of reproducing such a loading experimentally.

To address this challenge, a simple and accurate experimental set-up named as gap test was recently designed (Nguyen et al., 2020b,a). Fig. 1(a) shows the experimental set-up for the gap test. It involves compressible pads with nearly perfect plastic yielding to generate a crack parallel stress and rigid supports at beam ends with a gap set so that the pads yield before a bending moment is induced by the rigid supports. Fig. 1(b) depicts the representative deformation process.

The test can be divided into four stages. The plastic pads deform elastically in the first stage and yield in the second stage, which is a statically determinate situation. In the third stage, rigid supports start to produce a bending moment while the yield force in plastic pads remains constant as if it were a gravity load, and so the situation is again statically determinate. Finally, fracture occurs, and the load value returns to the plastic pad yielding load. The measured response of the plastic pad used later to define the constitutive equations of plastic pads in the numerical model is shown in Fig. 1(c). An important advantage of the gap test is that upon closing the gaps, the test setup switches from one statically determinate situation to another. This greatly simplifies the test evaluation and makes it unambiguous.

The load–displacement curve of the beam is illustrated in Fig. 1(d) and illustrates the aforementioned mechanism. The corresponding load-CTOD (crack tip opening displacement) curve of the beam under crack-parallel compression is shown in Fig. 1(e). The total fracture energy (G_F) can finally be calculated from the load–displacement response up to a large enough value of CTOD through the work-of-fracture method (Bazant and Planas, 2019), and the initial fracture energy (G_f) can be calculated by the size effect method, based on testing specimens of different sizes (Bažant and Kazemi, 1991; Cusatis and Cedolin, 2007; Cusatis and Schauffert, 2009).

The experimental setup of the gap test was numerically replicated in this study as closely as possible, as shown later on. Before introducing the gap test simulations, we first summarize the LDPM formulation.

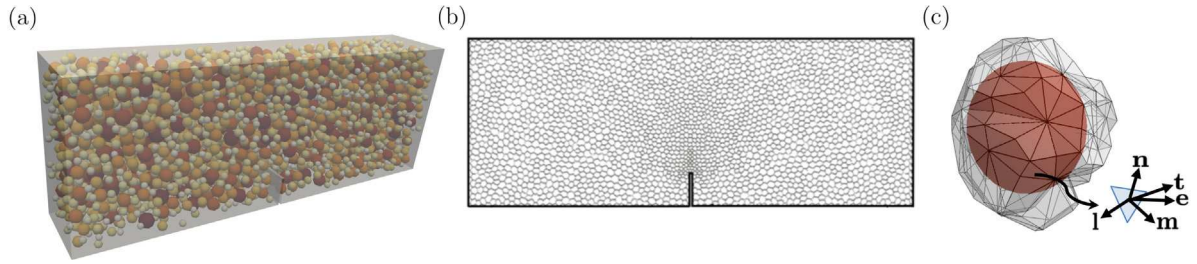

Fig. 2. LDPM internal geometry: (a) Particle placement; (b) LDPM cells; (c) Polyhedral cell around a coarse aggregate.

2.2. LDPM formulation

LDPM is a culmination of several decades of research. Its earliest predecessor is the 1987 model of Zubelewicz and Bažant; see Figure 2 in Zubelewicz and Bažant (1987). This was a two-dimensional (2D) model of contacting rigid polygonal particles generated not randomly but according to a photograph of the surface of a cut of concrete. The surface contacts were characterized by simple 2D stress–strain relations for normal and shear interactions and failure. The simulations of a notched specimen produced a wide curved damage band and pictures of distributed damage. But because of its oversimplifications, the model could not reproduce fracture and damage experiments. Attention then turned to truss-type damage models, which eventually proved to be totally inadequate. A random rigid-jointed frame-type lattice (Schlangen and Van Mier, 1992), whose beams resisted bending, led to significant but insufficient improvement in distributed fracturing modeling. It was realized that the improved lattice performance was due not to the beam bending, which made no sense physically, but to shear, namely the fact that the lattice connections transmitted shear and that the joints, or particles, had a rotational degree of freedom. So the bar lattices were abandoned, and the 1986 idea was resurrected, but in three dimensions and with a much more realistic 3D contact stress–strain relation with softening patterned after the successful microplane model M4 (Bažant et al., 2000). This led to the initial version of LDPM–at the time called the confinement-shear lattice (CSL) model–by Cusatis (2001). In the subsequent research (Cusatis et al., 2003a,b), the LDPM was gradually refined and generalized to its present powerful version (Cusatis et al., 2011b,a). Over the years, this model has been used to simulate fracture and size-effect (Pathirage et al., 2023a; Mercuri et al., 2023), behavior under cycling loading (Zhu et al., 2022), or other granular quasi-brittle materials such as mortar (Pathirage et al., 2019b; Han et al., 2020), fiber-reinforced concrete, and engineered cementitious composites (Schauffert and Cusatis, 2011; Rezakhani et al., 2021; Feng et al., 2022), unreinforced and reinforced stone masonry (Mercuri et al., 2020; Angiolilli et al., 2020, 2021; Mercuri et al., 2022, 2021), and shale (Li et al., 2017). LDPM was also coupled to multi-physics models describing cement hydration from microscale simulations (Pathirage et al., 2019a), heat transfer and moisture diffusion, alkali-silica reaction, creep, aging (Yang et al., 2021, 2022; Pathirage et al., 2023b), and more recently self-healing in concrete (Cibelli et al., 2022).

The LDPM simulates the fracture behavior of concrete at the length scale of major material heterogeneity (mineral aggregate particles). The geometrical representation of concrete mesostructure within the volume of interest is first constructed by randomly generating spherical particles based on the given cement content c, water-to-cement ratio w/c, aggregate-to-cement ratio a/c, maximum aggregate size d_a, and minimum simulated aggregate size d_0 (defining the resolution of the model), as shown in Fig. 2(a). Polyhedral cells (see Fig. 2(b)) are then created through a three-dimensional domain tessellation (Hang, 2015). These polyhedral cells interact by contacting triangular facets on the exterior of the polyhedral cells (see Fig. 2(c)). Discrete compatibility and constitutive equations explained in the following are finally defined on the facets (Cusatis et al., 2011b,a).

The facet strains are described (similarly to the microplane model Cusatis and Zhou, 2014; Lale et al., 2017) as follows:

$$e_N = \frac{\mathbf{n}^T[\![\mathbf{u}_C]\!]}{l};\ e_M = \frac{\mathbf{m}^T[\![\mathbf{u}_C]\!]}{l};\ e_L = \frac{\mathbf{l}^T[\![\mathbf{u}_C]\!]}{l}; \tag{1}$$

where $\mathbf{n}$ is a unit vector normal to the projected facet (Cusatis et al., 2011b), $\mathbf{m}$ and $\mathbf{l}$ are unit vectors of two mutually orthogonal components on the facets, $[\![\mathbf{u}_C]\!]$ is the displacement jump between the facets in the interface of two neighboring aggregate particles, and l is the length of the tetrahedron edge at the facet. In the elastic regime, the facet stress tractions are computed as:

$$t_N = E_N e_N\ ,\ t_M = E_T e_M\ ,\ t_L = E_T e_L \tag{2}$$

where E_N is the normal modulus and E_T is the shear modulus, which is equal to a shear-normal coupling parameter, α, multiplied by E_N. The normal modulus and shear-normal coupling parameters are related to the macroscopic elastic modulus and Poisson's ratio (Cusatis et al., 2011b).

Beyond the elastic limit, the damage (or fracturing) behavior for normal strains $e_N > 0$ under tension or tension with shear is characterized in terms of the effective strain, $e = [e_N^2 + \alpha(e_M^2 + e_L^2)]^{\frac{1}{2}}$, and the effective stress, $t = [t_N^2 + (t_M^2 + t_L^2)/\alpha]^{\frac{1}{2}}$. Based on the effective stresses and strains, the normal and shear stresses are then derived (Cusatis, 2001) as: $t_N = te_N/e$, $t_M = \alpha te_M/e$ and $t_L = \alpha te_L/e$. The effective stress t is incrementally elastic, defined as $\dot{t} = E_N\dot{e}$, and is limited by a strain-dependent boundary given by $0 \leqslant t \leqslant \sigma_{bt}(e,\omega)$ in which

$$\sigma_{bt}(e,\omega) = \sigma_0(\omega)\exp\left[-H_0(\omega)\frac{\langle e_{\max} - e_0(\omega)\rangle}{\sigma_0(\omega)}\right] \tag{3}$$

Here $\langle x\rangle = \max(x,0)$, ω is defined as $\tan(\omega) = (e_N)/(\sqrt{\alpha}e_T) = (t_N\sqrt{\alpha})/(t_T)$ where e_T is the total shear strain $e_T = (e_M^2 + e_L^2)^{\frac{1}{2}}$, and t_T is the total shear stress $t_T = (t_M^2 + t_L^2)^{\frac{1}{2}}$. Additionally, the maximum effective strain is a time-dependent variable that is defined as $e_{\max}(\tau) = [e_{N,\max}^2(\tau) + \alpha_0 e_{T,\max}^2(\tau)]^{\frac{1}{2}}$ where $e_{N,\max}(\tau) = \max_{\tau'<\tau}[e_N(\tau')]$ and $e_{T,\max}(\tau) = \max_{\tau'<\tau}[e_T(\tau')]$. The strength limit representing a smooth transition between pure tension and pure shear is given by:

$$\sigma_0(\omega) = \sigma_t \frac{-\sin(\omega) + (\sin^2(\omega) + 4\alpha_0\cos^2(\omega)/r_{st}^2)^{\frac{1}{2}}}{2\alpha_0\cos^2(\omega)/r_{st}^2} \tag{4}$$

where $r_{st} = \sigma_s/\sigma_t$ is the ratio of shear strength σ_s to tensile strength σ_t. When the maximum effective strain reaches its elastic limit, the effective softening modulus $H_0(\omega) = H_s/\alpha_0 + (H_t - H_s/\alpha_0)(2\omega/\pi)^{n_t}$, in which $H_t = 2E_0/(l_t/l - 1)$, $H_s = r_s E_0$ and n_t is the softening exponent, controls the post-peak softening modulus. The tensile characteristic length is calculated as $l_t = 2E_0G_t/\sigma_t^2$ (similar to Irwin's length), where G_t is the mesoscale fracture energy.

For compressive loading ($e_N < 0$), strain hardening plasticity is assumed, and the normal stress is limited by a strain-dependent stress boundary, $-\sigma_{bc}(e_D, e_V) \leqslant t_N \leqslant 0$, in which e_V is the volumetric strain, and e_D is the deviatoric strain. The evolution of strain-dependent stress boundary simulates the evolution of pore collapse, compaction, and re-hardening :

$$\sigma_{bc} = \begin{cases} \sigma_{c0} & -e_{DV} \leq 0 \\ \sigma_{c0} + \langle -e_{DV} - e_{c0}\rangle\, H_c(r_{DV}) & 0 \leqslant -e_{DV} \leqslant e_{c1} \\ \sigma_{c1}(r_{DV})\exp\left[\left(-e_{DV} - e_{c1}\right) H_c(r_{DV})/\sigma_{c1}(r_{DV})\right] & -e_{DV} > e_{c1} \end{cases} \tag{5}$$

where $r_{DV} = |e_D|/e_V$ for $e_V > 0$ and $r_{DV} = -|e_D|/(e_V - e_{V0})$ for $e_V \leq 0$ in which $e_{V0} = \kappa_{c3}e_{c0}$. $e_{c0} = \sigma_{c0}/E_0$ is the volumetric strain at the onset of pore collapse; σ_{c0} is the mesoscale yielding compressive stress; $e_{c1} = \kappa_{c0}e_{c0}$ is the strain at which the rehardening starts; and κ_{c0}, κ_{c3} are material parameters. $\sigma_{c1}(r_{DV}) = \sigma_{c0} + (e_{c1} - e_{c0})H_c(r_{DV})$ in which $H_c(r_{DV})$ is defined as $H_c(r_{DV}) = H_{c1} + (H_{c0} - H_{c1})/(1 + \kappa_{c2}\langle r_{DV} - k_{c1}\rangle)$ where H_{c0}, H_{c1}, κ_{c1} and κ_{c2} are material parameters. In the presence of compressive stresses, frictional effects lead to an increase in the shear strength, which is described by a nonlinear Mohr–Coulomb model in which the internal friction coefficient decreases from an initial value μ_0 to 0. This is formulated as $\sigma_{bs} = \sigma_s + \mu_0\sigma_{N0}[1 - \exp(\sigma_N/\sigma_{N0})]$ where σ_s is the cohesion, and σ_{N0} is the transitional stress.

For a correct prediction of the gap test response, the following model parameters need to be carefully identified: (1) E_0 and α that govern the elastic behavior; (2) σ_{c0}, H_{c0}/E_0, and κ_{c0} that govern compression under confinement (identified by fitting a hydrostatic test); and, finally, (3) σ_t, G_t, and σ_s that govern tensile/shear softening behaviors (identified by fitting tensile fracture tests and unconfined compression tests). The quantification of the influence of these material parameters corresponding to different experimental tests can be found in Ref. Lyu et al. (2023).

2.3. Experimental data and LDPM simulations

2.3.1. Description of Nguyen et al.' experiments

In the experimental program of Nguyen et al. (2020b,a), the concrete mix had cement content $c = 338.168\ \mathrm{kg/m^3}$, water-to-cement ratio $w/c = 0.45$, and maximum aggregate diameter $d_a = 18$ mm. To characterize the material, standard unconfined compression tests on prisms of dimensions $76.2 \times 76.2 \times 152.4$ mm were performed, along with Brazilian splitting tests on cylinders of diameter 101.6 mm and length 203.2 mm, and four-point bending (4PB) tests. The gap tests were carried out for different crack-parallel compressive stress levels and for small, medium, and large specimen sizes. Each beam had a span-to-depth ratio of 3.75 and a notch-to-depth ratio of 0.3. All the beams had 3-mm-wide notches. The beam depths were 101.6 mm (small), 203.2 mm (medium), and 406.4 mm (large), and the width was 101.6 mm for all sizes. The elasto-plastic pads had three depths for the three different specimen sizes, 25.4, 50.8, and 101.6 mm. The width was equal to the width of the specimen (101.6 mm).

The identification of σ_{c0}, H_{c0}/E_0, and κ_{c0} required hydrostatic compression test data. However, the original experimental work (Nguyen et al., 2020a) did not include hydrostatic tests. Therefore, experimental data on similar concretes were taken from the literature to obtain a set of material data sufficient for parameter identification. For this purpose, the data on hydrostatic tests on cylinders (65.58 mm diameter × 131.1 mm length) reported by Green and Swanson (1973) were chosen because the mix design and compressive strength were similar to the ones used in the gap tests (Nguyen et al., 2020a). However, the elastic properties in Ref. Green and Swanson (1973) differed from those in Nguyen et al. (2020a).

Hence, the hydrostatic stress–strain curve was corrected as follows. If one defines ε_V^{true}, σ_V^{true}, and κ^{true} as the desired volumetric strain, volumetric stress, and the volumetric modulus of the ε_V^{true} vs. σ_V^{true} curve, the desired volumetric strain can then be calculated as $\varepsilon_V^{true} = \varepsilon_V^0 - \sigma_V^0/\kappa^0 + \sigma_V^0/\kappa^{true}$ and $\sigma_V^{true} = \sigma_V^0$, where ε_V^0, σ_V^0 and κ^0 are, respectively, the volumetric strain, volumetric stress, and the volumetric modulus of the experimental data in Ref. Green and Swanson (1973).

2.3.2. Modeling details

The LDPM mesostructure was constructed using the given experimental mix design, Fuller coefficient $n_F = 0.5$, and the minimum aggregate size, $d_0 = 5$ mm. LDPM simulations of hydrostatic tests, uniaxial compression tests, 4PB tests, Brazilian splitting tests, and gap tests were conducted. The 4PB tests were simulated by using LDPM in the central portion of the specimens and elastic 8-node brick finite elements for the other parts of the model.

Hydrostatic test: Fig. 3(a) shows the schematic configuration of the hydrostatic test. A surface-based contact was utilized to simulate the interfaces, viz., the interface between the loading platen and concrete cylinder and the interface between the steel

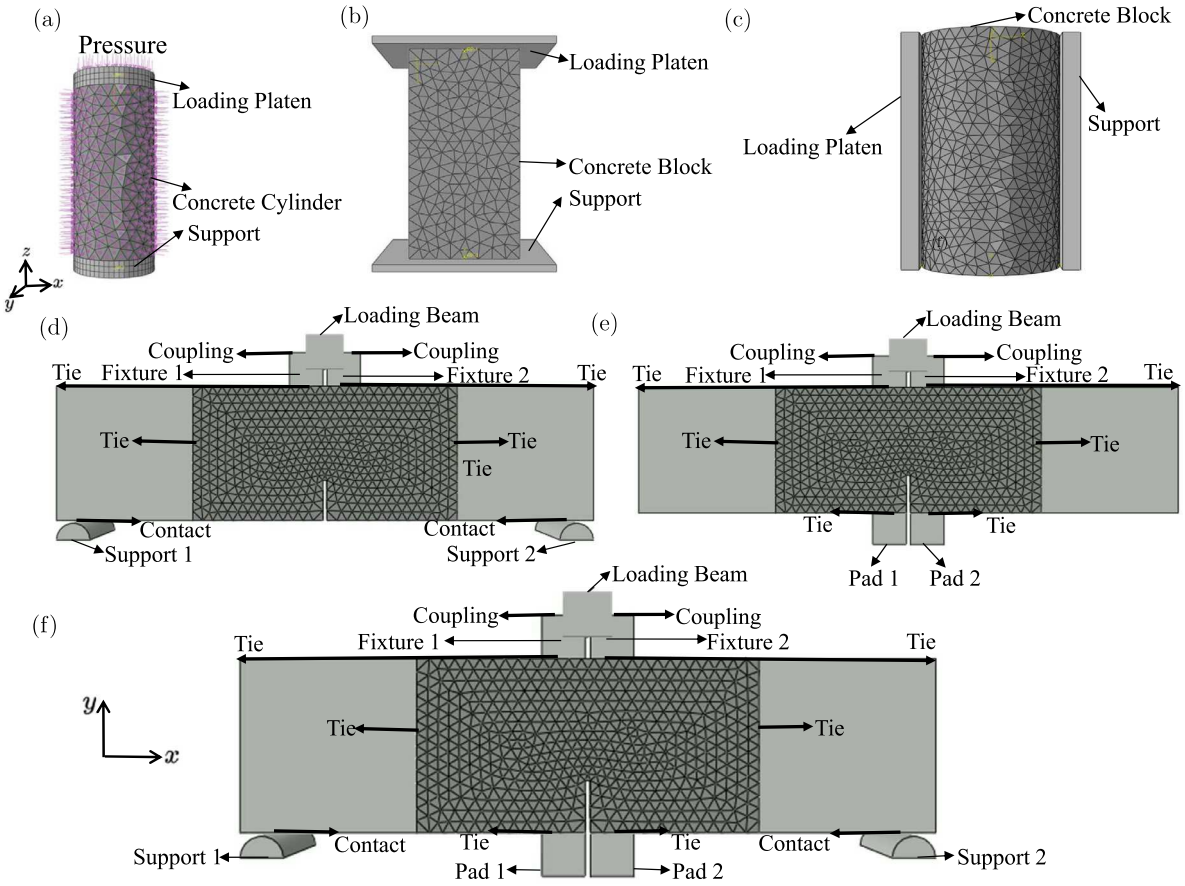

Fig. 3. LDPM setup for (a) hydrostatic test; (b) unconfined compression test; (c) Brazilian test; (d) 4PB test.

support and concrete cylinder. Concerning the contact properties, a "hard" contact option for "pressure-over closure" was utilized for the normal contact behavior (Manual, 2012). This aimed to avoid the penetration of the secondary surface into the primary surface at the constraint locations and the transfer of tensile stress across the interface. The classical Coulomb friction law with a friction coefficient of $\mu = 0.13$ defined the tangential contact behavior.

Uniaxial compression test: Fig. 3(b) shows the uniaxial compression test. Similar to the hydrostatic test, the surface-based contact simulating the interfaces and "hard" contact defining the normal contact behavior were still utilized. However, the static and dynamic friction parameters described in Ref. Cusatis et al. (2011a) were used for simulating frictional effects between steel loading platens and concrete specimen ends.

Brazilian splitting test: For the Brazilian test, Fig. 3(c), the same contact properties as in hydrostatic tests were used to define the interfaces.

4PB test: For the 4PB test shown in Fig. 3(d), a kinematic coupling was used to link the degrees of freedom (DOFs) of two endpoints of the loading beam with two reference points in fixture 1 and fixture 2, respectively, so that these two reference points shared the same displacement with the middle point of the beam. It should be pointed out that the loading beam was considered rigid. Additionally, the nodes at the middle line of the top surface of fixtures 1 and 2 were paired with reference points in them, respectively, to define constraint equations such that the paired nodes shared the same displacement and rotation. The bottom surfaces of fixtures 1 and 2 were tied to the top surface of the concrete beam instead of applying contact interactions between the surfaces. In the tie constraints, each node on the secondary surface (concrete beam) was constrained to have the same displacement as the corresponding points on the primary surfaces (fixture 1 and fixture 2). Additionally, since the damage was expected to appear near the tip of the notch, only a certain width of the central portion of the specimens (200 mm, 400 mm, and 800 mm for the small, medium, and large beam, respectively) was used for LDPM to save computational cost. The lateral portions were connected to the LDPM region through the tie constraint. The side cracking was avoided by tying a 2 mm thick laminate layer to the bottom surface of the concrete beam since, in the experiment, such a layer was glued to the bottom surface of the concrete beams. For the interfaces between the concrete beam and support 1 and between the concrete beam and support 2, the same contact properties as that described for the hydrostatic test were used.

Compressive failure test: To compute the crack-parallel stress level (σ_C) that causes compressive failure, the setup illustrated in Fig. 3(e) was simulated. The pads were defined as a linear elastic material so as to ensure that concrete failure occurred before the

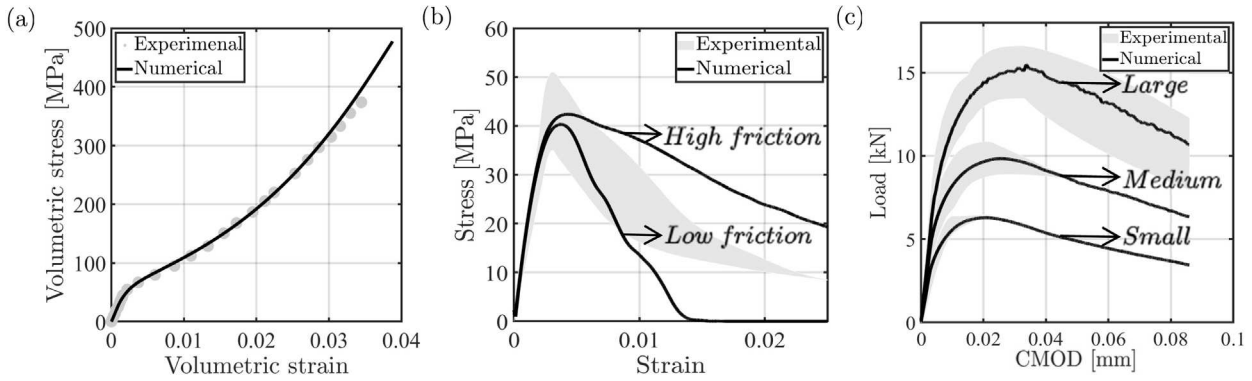

Fig. 4. LDPM simulation for (a) hydrostatic compression; (b) uniaxial compression; (c) fracture behavior. The gray line represents the experimental curve, and the black line represents the average response from six models.

yielding of the pads. The pad's elastic properties were obtained from the compression tests of the pads. Compared with the 4PB test setup in Fig. 3(d), one can point out that two pads are added to the setup while removing the two steel supports at the bottom. The pad and concrete beam interface were fully bonded together through the tie constraint.

Gap test: Fig. 3(f) shows the whole setup of the gap test. As mentioned, two steel supports were added to the setup while leaving a gap between the support and concrete beam compared with Fig. 3(e). A general contact algorithm available in typical FEA software (Manual, 2012) was used to model the support and concrete beam interfaces. When general contact is used, many contact pairs can be defined simultaneously, and the contact region is not necessarily continuous as in the case of surface-to-surface contact. The hard contact option, in which the contact constraint begins to work when the clearance between the two surfaces becomes zero, was used for the normal behavior, and the penalty with a small friction coefficient of 0.003 was used for the tangential behavior. The nearly perfect plastic properties of the pads were defined based on experiments.

To make the gap test simulations replicate the exact experimental conditions as closely as possible, one needs to pay attention to several details in the modeling process. First, all the parts except the part simulated by LDPM should be meshed using elements with full integration since reduced integration using a lesser number of Gaussian coordinates for solving the integral always led to instability of the simulations. Second, a mesh convergence study was performed for different mesh sizes for the plastic pads. It was found that refining the mesh of the plastic pads so as to have at least six elements through its thickness was optimal in terms of computing time and accuracy. Third, the kinematic coupling instead of a tie constraint was used when linking the DOFs of the two endpoints of the rigid loading beam with two reference points in fixture 1 and fixture 2, respectively. The reason was that a coupling aimed to provide a constraint between a reference node and the nodes on a surface works well, especially when a group of coupling nodes is constrained to the motion of a single node. Next, only the nodes at the middle line of the top surfaces of fixture 1 and fixture 2, instead of the nodes on the entire surface, shared the same displacement and rotation with their two reference points, respectively. Finally, it is known that instabilities may appear when discontinuous stiffness changes due to the nature of contact defined by normal and tangential behaviors. A tie constraint was used to attach the plastic pads to the laminate and tie the concrete beam to the fixtures to avoid this instability. The corresponding boundary conditions were applied to define only the movement of plastic pads and fixtures along the y-direction instead of defining all their DOFs.

3. Identification of model parameters and model predictions

3.1. LDPM parameters calibration

The material parameters that define the elastic behavior, hydrostatic compression behavior, softening tensile fracturing behavior, and macroscopic behavior in compression (σ_{c0}, H_{c0}, κ_{c0}, σ_t, G_t, σ_s) were identified from a combination of the hydrostatic test, unconfined compression test, and fracture test. The relative accuracy of the set of material parameters was visually assessed by fitting simulation results to the experimental response curves. Additionally, it should be pointed out that the remaining parameters were identified in previous works (Cusatis et al., 2011a; Alnaggar et al., 2013) and that they do not change significantly for standard concrete mixes: $n_t = 0.2$, $r_s = 0$, $\kappa_{c1} = 1$, $\kappa_{c2} = 5$, $\kappa_{c3} = 0.1$, $\mu_0 = 0.2$, $\sigma_{N0} = 600$ MPa, $H_{c1}/E_0 = 0.1$, and $E_d/E_0 = 1$. The procedure to calibrate the relevant parameters is provided below.

First, $E_0 = 31056$ MPa and $\alpha = 0.25$ were computed using the elastic response from uni-axial compression tests. Next, the volumetric stress–strain curve for the hydrostatic test was considered to identify parameters related to hydrostatic compression. The parameters of interest here were σ_{c0}, H_{c0}/E_N, and κ_{c0}. The following values were obtained: $\sigma_{c0} = 60$ MPa, $H_{c0}/E_0 = 0.15$, $\kappa_{c0} = 4.5$. Fig. 4(a) shows the comparison between the experimental and numerical volumetric stress–strain data. In this case, the gray line represents the experimental curve, and the black line represents the average response from three random spatial distributions of particles. It can be seen that the numerical response obtained by the identified parameters matches well the experimental data.

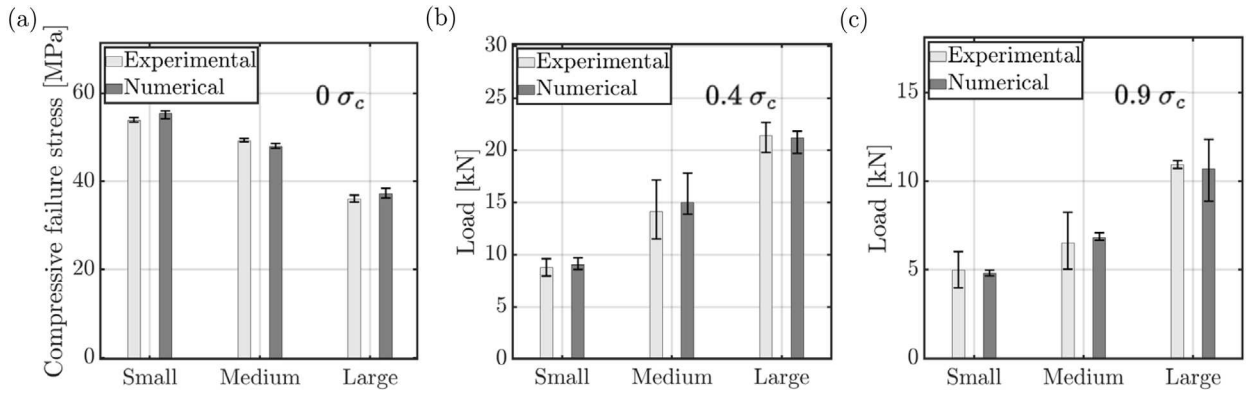

Fig. 5. Comparison between the experimental and numerical data for the (a) compressive failure stress; (b) peak at 0.4 σ_C; (c) peak at 0.9 σ_C.

The remaining parameters σ_t, G_t, and σ_s/σ_t were finally identified such that the output of the simulations agreed simultaneously with the experimental stress–strain curve from the uniaxial compressive test, and with the load–CMOD (crack mouth opening displacement) curves obtained from the 4PB test of the small, medium, and large specimens. The resulting parameters were $\sigma_t = 4.7$ MPa, $G_t = 30$ N m^{-1} and $\sigma_s/\sigma_t = 3.1$. The results for the fracturing behavior and compressive strength are shown in Fig. 4(b) and (c). Since the frictional coefficient between the loading platens and the specimen in the compression tests is unknown, both low friction and high friction parameters described in Cusatis et al. (2011a) were used in the numerical simulations. Fig. 4(b) shows that the experimental curves lie in between the numerical responses for low and high friction. Fig. 4(c) further confirms that the numerical load-CTOD curves for the small, medium, and large notched specimens match well the experimental result.

3.2. LDPM predictions

The calibrated model was used to predict and compare the responses in the Brazilian tests, compressive failure tests, and fracture tests with different crack-parallel stress levels.

3.2.1. Splitting tensile and compressive failure tests

The value of the predicted splitting tensile strength was compared with the experimental one, and the relative error was about 1%.

Before analyzing the gap tests, the value of crack-parallel stress σ_C that causes compressive failure in the setup shown in Fig. 3(e) must be determined for comparison. Fig. 5(a) compares the value of σ_C. Excellent agreement between the experimental and numerical results is seen in the figure. The error bars in the figure represent the range from the minimum to the maximum response.

3.2.2. Fracture tests with crack-parallel stresses

Next, the peak loads measured on these specimens at $0.4\sigma_C$ and $0.9\sigma_C$ reported experimentally were compared with the LDPM simulations. The results are shown in Fig. 5(b) and (c). One can observe that the peaks from LDPM predictions are in good agreement with the experimental results. Note that thanks to using the size effect method (Shah, 1990; Bažant et al., 2021), only the peak load of specimens of various sizes had to be measured to characterize the initial fracture energy G_f of the material. Additionally, for the same reason, the experiments did not have to be, and were not, properly stabilized to observe the post-peak as seen in Fig. 6. Fig. 6 shows the load/CTOD (crack tip opening displacement) comparisons for different specimens with different levels of crack-parallel stress. As noted, some experimental data for the load-CTOD curves are unavailable, so only the peak was provided.

4. Results and discussion

4.1. Effects of crack-parallel stress on G_f and c_f

According to Bažant's size-effect law (SEL), the relation between $1/\sigma_N^2$ and D can be written as:

$$\frac{1}{\sigma_N^2} = \frac{g(\alpha_0)}{EG_f} D + \frac{g'(\alpha_0)}{EG_f} c_f \tag{6}$$

where $\sigma_N = P/bD$, P is the peak load, b is the beam thickness, D is the beam depth, E is the elastic modulus, G_f is the initial fracture energy, c_f is the critical effective crack extension, $g(\alpha_0)$ represents the non-dimensional energy release rate, and $g'(\alpha_0)$ is the

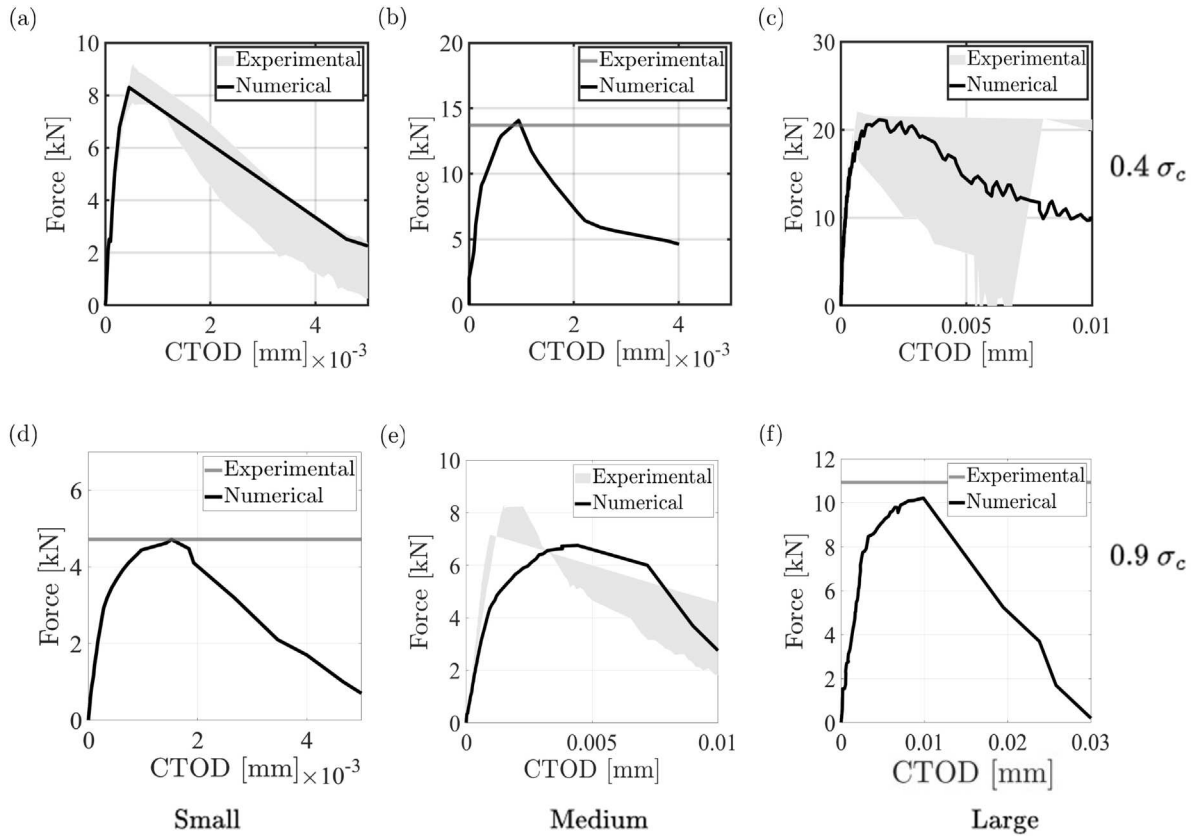

Fig. 6. Load-CTOD comparisons between the experimental and numerical data for the (a) small size with 0.4 σ_C, (b) medium size with 0.4 σ_C, (c) large size with 0.4 σ_C; (d) small size with 0.9 σ_C, (e) medium size with 0.9 σ_C, (f) large size with 0.9 σ_C.

derivative of $g(\alpha_0)$ at α_0 (α_0 = notch depth/beam depth) (Bažant and Planas, 2019). For the present geometry, the non-dimensional energy release rate is:

$$g(\alpha_0) = \left(1.1682(2h - s)\sqrt{\pi\alpha}/(8\beta^{3/2}) \left[5 - 10\alpha/3 + \alpha^2 + 40\alpha^2(1-\alpha)^6 + 3\exp\left(\frac{-6.134\alpha}{1-\alpha} \right) \right] \right)^2 \tag{7}$$

in which $h = L/D$, $s = S/D$, and $\beta = 1 - \alpha_0$. In the above equations, L represents the half-span length between the supports, and S represents the distance between the two center-span loads (Nguyen et al., 2020a). Hence, plotting $1/\sigma_N^2$ vs. D, one may compute slope A and intercept C of the corresponding linear regression. The fracture energy, G_f, and the critical effective crack extension, c_f, can then be calculated from the slope A and intercept C of the linear regression plot using the following equations (Gettu et al., 1998; Ince, 2010; Cedolin and Cusatis, 2007; Bažant, 1999):

$$G_f = \frac{g(\alpha_0)}{AE} \quad \text{and} \quad c_f = \frac{Cg(\alpha_0)}{Ag'(\alpha_0)} \tag{8}$$

Fig. 7(a)–(c) show the size effect curves for crack-parallel stresses $\sigma_{xx} = 0$, $0.4\sigma_C$ and $0.9\sigma_C$. The black dots and lines represent the computed values and the size-effect law, respectively, whereas the gray color shows experimental results. For the unconfined and medium confinement cases, the experimental data points and LDPM data points are almost exactly aligned on a straight line. This is consistent with the SEL. For confinement of $0.9\sigma_C$, the deviation from the linearity is significant. This is the first indication that the fracture mechanisms at high confinement are different than they are at lower values.

Table 1 shows the calculated values of G_f and c_f for both numerical predictions and experiments. It can be observed that G_f increased to about two times for $0.4\sigma_C$ stress, and G_f decreased by up to 41% for $0.9\sigma_C$ stress when compared with those obtained from zero stress both experimentally and numerically. It may immediately be noticed that LDPM gives a closer agreement with the point for $0.4\sigma_C$ than does the crack band model (CBM) used in the original gap test study (Nguyen et al., 2020a). The reason, anticipated in Nguyen et al. (2020b), is that the width of the FPZ in the CBM used in Nguyen et al. (2020a) is fixed, while in LDPM it can increase. However, in the new model (completed after the present study), the smooth crack band model (sCBM) (Zhang and Bažant, 2023) (with sprain energy), the FPZ width can also increase. On that note, it is worth mentioning that the Concrete Damage Plasticity Model 2 (CDPM2) developed by Grassl et al. (2013) might be able to capture crack-parallel stress effect thanks

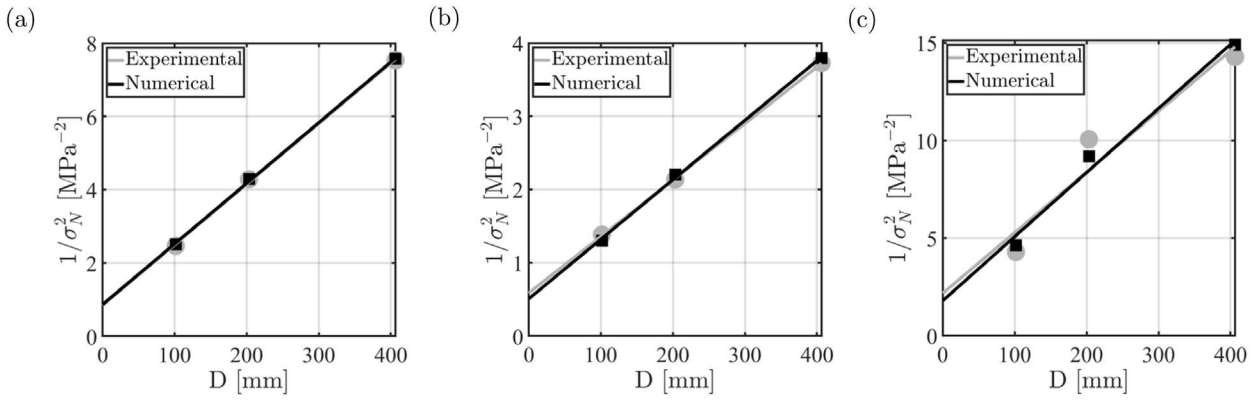

Fig. 7. Linear regression of size effect method for crack-parallel stress of (a) 0; (b) $0.4\sigma_C$; (c) $0.9\sigma_C$. The black dots and lines represent the numerical values and the fitting of the size-effect law, respectively, whereas the white color refers to experimental results.

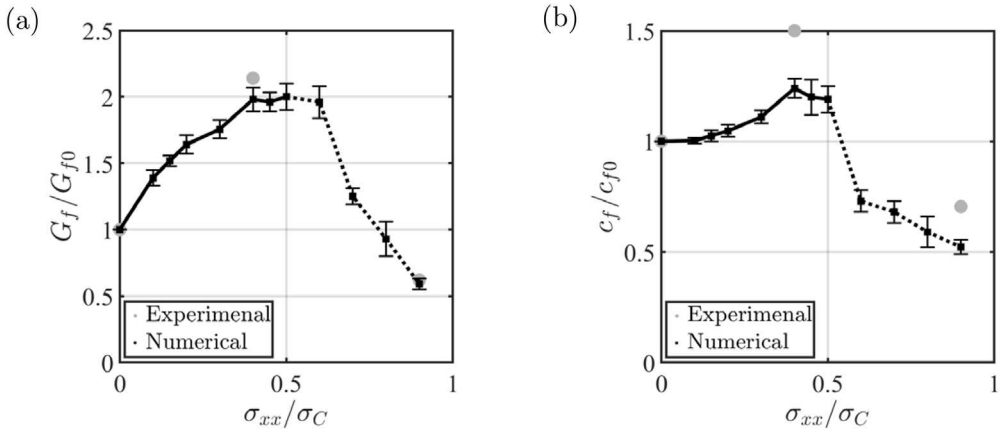

Fig. 8. (a) G_f as a function of the ratio of σ_{xx} and σ_C; (b) c_f as a function of the ratio of σ_{xx} and σ_C.

Table 1
Calculated G_f and c_f from the experimental and numerical results.

Pressure	G_f from experiment (N/m)	G_f from simulation (N/m)	c_f from experiment (mm)	c_f from simulation (mm)
0	86.3	86.2	20	21.07
$0.4\sigma_C$	185	171	30	26
$0.9\sigma_C$	53.4	50.5	14.1	11

to the model's tensorial nature. The LDPM slightly underestimates c_f with respect to experimental data, which might be due to insufficient experimental data points — only three tests per loading case. Additionally, several LDPM simulations with different ratios of applied crack-parallel stress σ_{xx}/σ_C were performed to capture the changing trend of fracture parameters with different crack-parallel stress levels. Six to eight simulations with different particle distributions were performed for each ratio. Fig. 8(a) and (b) show the evolution of G_f and c_f as a function of σ_{xx}/σ_C.

As confirmed by this study, fracture parameters, G_f and c_f, are highly dependent on the crack-parallel stress levels, and the opposite trend is seen between moderate and high crack-parallel stress. Based on the above analysis, one can confirm the previous conclusion in Nguyen et al. (2020a,b) that fracture parameters can either increase or decrease according to the crack-parallel stress level. This limits the applicability of standard fracture models with constant fracture energy G_f (or constant critical K_c) to situations where crack-parallel stresses are negligible. Such cases are rare in practice (the Liberty Ships fractures in the 1940s were one rare exception).

In view of the finite and varying fracture front width, some scholars might question the use of the SEL. Indeed, the best-known and mathematically cleanest derivation of the SEL is based on deviations from linear elastic fracture mechanics of line cracks caused by a cohesive zone of finite length at the crack tip (Bažant, 1990). Here, by contrast, we consider an FPZ of finite width. But suspecting that this may invalidate the use of SEL would be a misconception. The original derivation of the SEL in 1984 (Bažant, 1984), albeit

quite simplified, was based on the change of the energy release rate due to the widening, rather than lengthening, of the crack front. This was later invoked in more detail in the discussion of Fig. 12.8 in Bažant and Cedolin (1991), and Fig. 1.b in Bažant (2002a). A fundamental explanation lies in the thermodynamic concept of configurational forces, as applied to widening crack front by Herrmann and Sosa (1986) and Kienzler and Herrmann (1986) and improved in Bažant (1990). It appears that the width of the FPZ has an equivalent effect on the transitional form of the energetic size effect law as the length of the FPZ adds, and both are proportional to the SEL parameter c_f. But the application of the concept of configurational forces to the crack front width changes still awaits a predictive general calculation of the ratio of equivalent fracture length and width increases (Bažant, 1990), which is not exactly equal to 1.

Remark. One might object that the foregoing argument might not apply when the effective size c_f of the FPZ decreases with increasing crack parallel compression σ_{xx}, which occurs when approximately $-\sigma_{xx} > 0.5\sigma_c$. Here two points should be noted: (1) The fracture energy depends only on the extrapolation of the size effect law to infinite size, i.e., on the location of the asymptote of slope $-1/2$ in the log–log plot, which is determined with the help of dimensional analysis as shown in Bazoant et al. (1986) and has nothing to do with the second-order asymptotic matching that yielded the estimate of c_f (Bažant and Kazemi, 1990). (2) When c_f begins to decrease with increasing crack-parallel compression, the decrease cannot be interpreted as a narrowing width of the FPZ. Rather, the decrease means that the frictional damage dissipative mechanism is getting suppressed and transits to axial compression splitting which is not part of the second-order asymptotics (Bažant et al., 2021) that led to the estimation of c_f. A more refined asymptotic theory would have to be developed, which is beyond the scope of this paper.

4.2. Effects of crack-parallel stress on fracture process zone size at peak load

The dissipated energy density, defined as the free energy dissipated per unit volume of material, was post-processed from the LDPM numerical simulations to characterize the FPZ. In LDPM, the rate of dissipated energy density for each facet can be calculated as $\dot{w}_d = 3Al\left(t_N\dot{e}_N^{ine} + t_M\dot{e}_M^{ine} + t_L\dot{e}_L^{ine}\right)$ in which e_N^{ine}, e_M^{ine}, and e_L^{ine} correspond to the inelastic strains along orthogonal directions M, N, L (Pathirage et al., 2023a). To characterize the FPZ, the specimen was then subdivided into a rectangular grid of cells with x-and y-edge lengths of 5 mm. The energy densities dissipated in these cells were determined by calculating the dissipated energy on all facets located within each grid cell and dividing these energy values by the volume of each cell.

The average dissipated energy density in the x-direction was obtained by integrating the density in the y-direction divided by the beam depth. The dissipated energy density along the y-direction, parallel to the crack, was obtained by integrating the dissipated energy densities along the x-direction divided by the beam length. Fig. 9 shows the contour plot for different sizes and levels of crack-parallel stress. As seen, the evolution of the FPZ width and length as the specimen size, D, are increased for different levels of crack-parallel stress. The FPZ width and length increase with the increase of the specimen size. This means that, generally, more energy was dissipated for larger sizes. In this case, the FPZ was not fully developed even for the 400 mm depth. When the FPZ develops fully, the spread and density of the dissipated energy should be almost the same for different sizes. Hence, to obtain a fully developed FPZ, beams with a depth larger than 400 mm should have been used.

Comparing the FPZ sizes for different crack-parallel stresses at the same beam depth indicates that the FPZ width and length increase when the pressure is increased from 0 to $0.4\sigma_c$. This is due to the propagation of microcracking and frictional micro-slips caused by the increase of static friction as the pressure increases, which builds up a larger FPZ. When the pressure increases from $0.4\sigma_c$ to $0.9\sigma_c$, the FPZ width still increases at no increase in its length, which is due to interparticle frictional slips on inclined planes after the static friction gets overcome (Bažant et al., 2022b). This softens the damage zone, causing it to expand laterally. This eventually leads to FPZ collapse by axial compression rather than by Mode I fracture, which explains why the Mode I fracture energy decreases towards zero. Doubtless, this is because the increasing crack-parallel compression needs first to overcome static friction and cause slip on the inclined microcracks, and these slips cause the FPZ to expand laterally while the FPZ length remains unaffected (Bažant et al., 2022b).

Fig. 10 shows the normalized FPZ width and length versus the normalized size where $X = \left(g_0 D\right) / \left(g_0' l_{\mathrm{f}}\right)$ and Y is the FPZ width or length normalized by l_f, in which $l_f = 2EG_f/f_t^2$, f_t is the tensile strength. Note that the values of X are in the range in which cohesive crack analysis, too, predicts that the FPZ is not yet fully developed (Cusatis and Schauffert, 2009). The fact that the width and length of the FPZ for $0.9\sigma_c$ confinement might seem to contradict the decrease of c_f has already been explained in the foregoing. It is due to the transition of mode I fracture to compression splitting fracture. This is analyzed again in detail in the next section.

4.3. Dissipation mechanisms in the fracture process zone

Since the crack patterns showed a similar trend for different specimen sizes, only the crack distribution for the medium samples is analyzed here. Fig. 11 shows, for the medium-size specimens, the crack evolution from peak to the post-peak with $\sigma_{xx} = 0$, $0.4\sigma_c$ and $0.9\sigma_c$. It can be seen that the crack evolves from a single crack band attachment at the notch tip (at zero stress) to one that resembles the occurrence of shear bands (at $0.9\sigma_c$), and higher confinement causes a more significant damage area than that without parallel stress.

Fig. 12(a), (b), and (c) present the normalized dissipated energy for different mechanisms, calculated by normalizing the dissipated energy for different mechanisms relative to the total dissipated energy for the medium-size specimen with different pressures. The dissipated energy was calculated from the increment of the dissipated energy calculated at LDPM facets divided

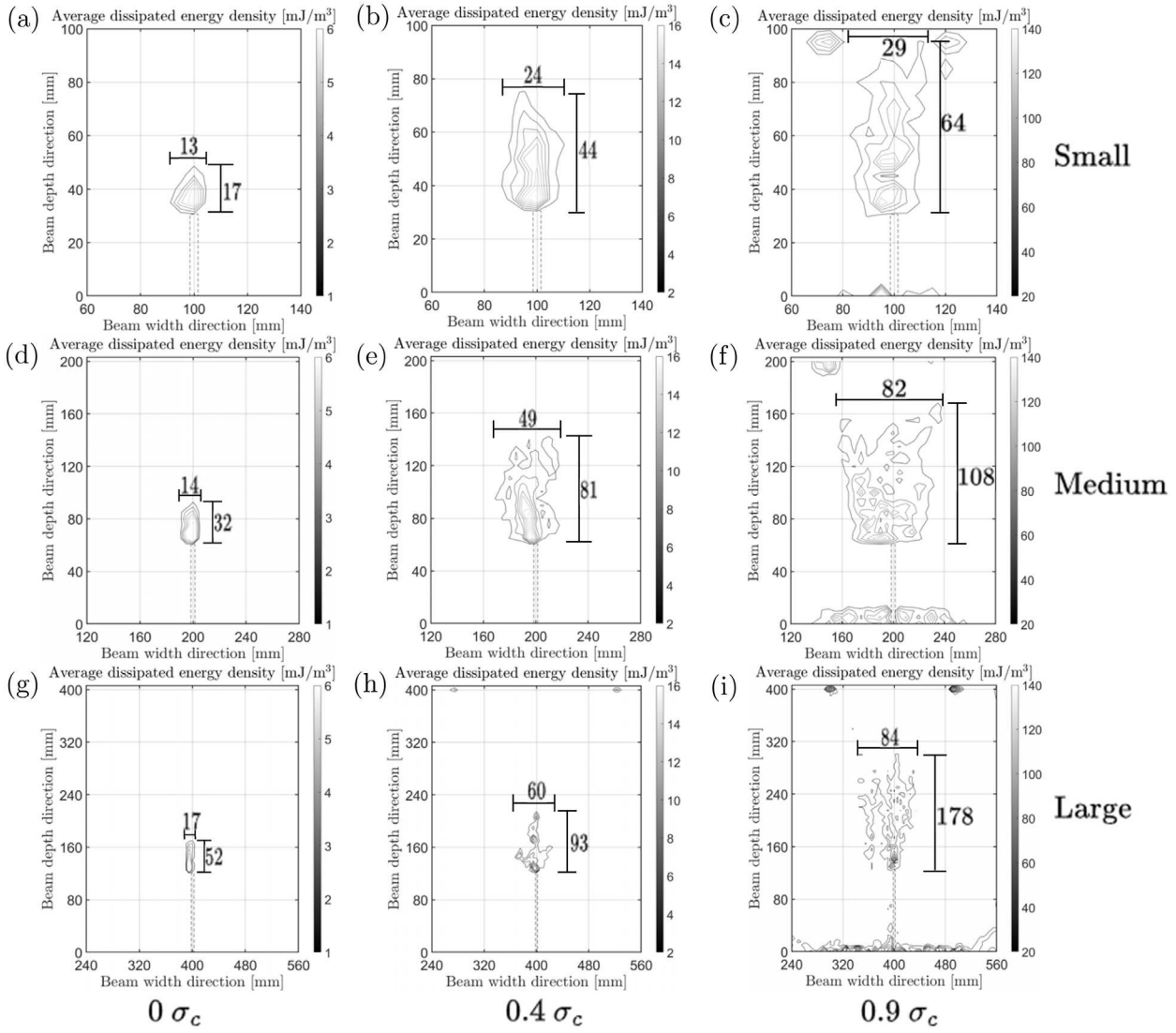

Fig. 9. Average dissipated energy density contour plot for different sizes and levels of crack-parallel stress.

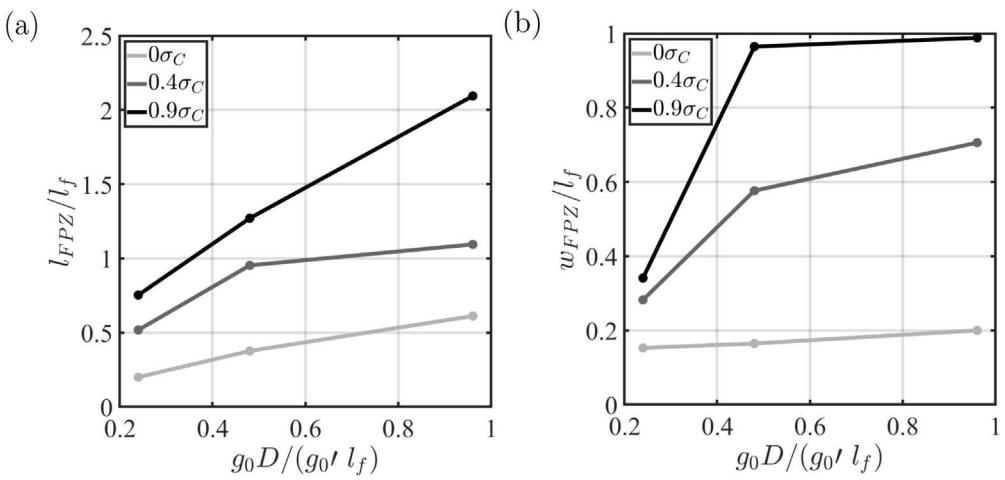

Fig. 10. Linear softening: (a) FPZ length at peak load; (b) FPZ width at peak load.

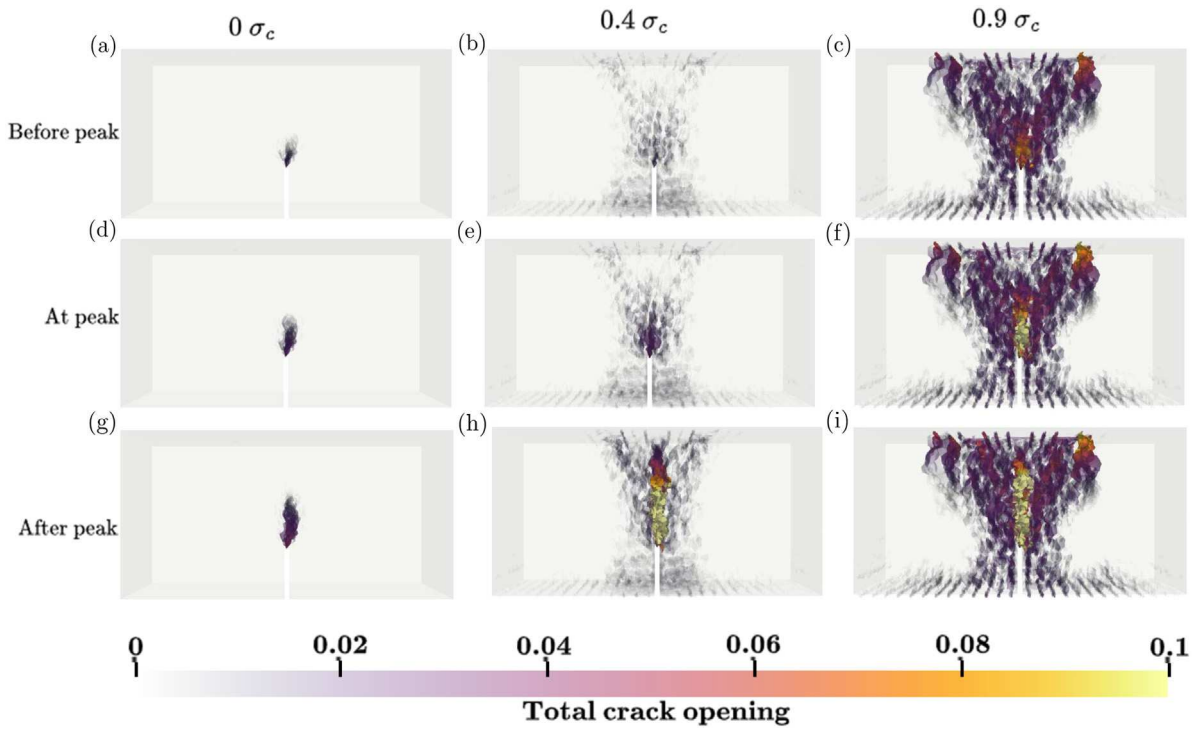

Fig. 11. Crack evolution from pre-peak to post-peak for the medium samples.

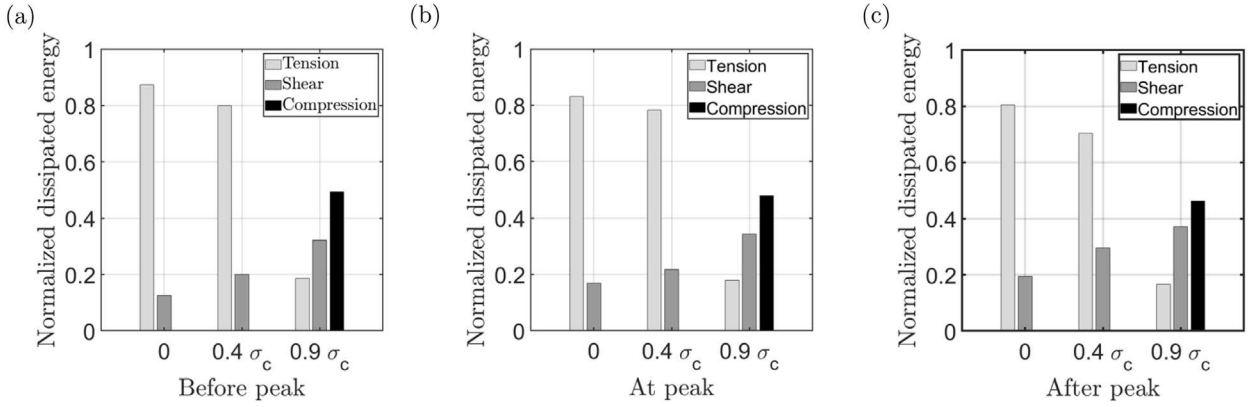

Fig. 12. Normalized dissipated energy for the medium samples with (a) $0\sigma_c$, (b) $0.4\sigma_c$, (b) $0.9\sigma_c$.

by the volume of the cell containing the corresponding facets. In LDPM, one can distinguish three types of failure mechanisms and associated dissipated energy: the energy dissipated in shear, in tension, and in compression. The rate of energy dissipated in shear is calculated as $\dot{w}_{dS} = 3Al\left(t_M \dot{e}_M^{ine} + t_L \dot{e}_L^{ine}\right)$. The rate of energy dissipated in tension is calculated as $\dot{w}_{dT} = 3Alt_N \dot{e}_N^{ine}$ for $e_N > 0$ whereas the rate of energy dissipated in compression is computed as the rate of the total energy dissipated in the normal direction minus the rate of energy dissipated in tension. From the dissipated energy rate, the total dissipated energy is calculated by integration in time.

The normalized dissipated energy for different failure mechanisms is here plotted for pre-peak, at the peak, and after the peak load. One can observe that the fraction of the energy dissipated under compression is nearly near zero when the crack-parallel stresses are 0 and $0.4\sigma_c$. However, the compression-dissipated energy dominates when the crack-parallel stress reaches $0.9\sigma_c$. Also, the fraction of the energy dissipated in shear increases with increasing confinement. This demonstrates that the failure mode changes with increasing confinement.

5. Conclusions

The present numerical analysis of gap tests confirms that crack-parallel compression has important effects on the fracture behavior of concrete. The relevant LDPM parameters were first calibrated by the experimental data on compression tests and by 4PB tests. They were then validated by simulating splitting and gap tests with 0, $0.4\sigma_c$, and $0.9\sigma_c$ confinement. It can be seen that when identifying LDPM material parameters, a systematic calibration procedure can be devised based on specific experimental tests and failure mechanisms, and the identified material parameters can make remarkable predictions. The following conclusions can be drawn:

1. The value of fracture energy G_f obtained through the size-effect method from the numerical simulations matches the value obtained from the experimental data. G_f strongly depends on the crack-parallel stress. An increasing trend for the moderate crack-parallel stress ($0.4\sigma_c$) and a decreasing trend for high crack-parallel stress ($0.9\sigma_c$) observed experimentally are here confirmed numerically.
2. For both the zero and high crack-parallel stresses, the numerically found value, c_f, characterizing the effective fracture process zone width, is in good agreement with the one obtained experimentally. The c_f is slightly underestimated for moderate crack-parallel stress. The classical crack band model (CBM), having a fixed bandwidth, inevitably underestimates it more, but the smooth crack band model (sCBM) just completed can simulate the width increase.
3. The FPZ width and length have been estimated in LDPM by computing the average dissipated energies. The results indicate that the FPZ width and length increase with structural size regardless of the crack-parallel stress level. In other words, unless the FPZ is fully developed, the energy dissipation is size-dependent.
4. Additionally, for a given structure size, the level of crack-parallel stress affects the FPZ size. The FPZ width and length increase with the increase of the magnitude of compressive crack-parallel stress. Up to the moderate levels of crack-parallel compressive stress, this agrees well with the trend of c_f. For high levels, the trends disagree which is probably due to the emergence of crack-parallel splitting.
5. For compressive stress higher than $0.5\sigma_c$, the failure mechanism changes from frictional damage to compression splitting cracks.
6. The relative proportion of the energy dissipated by the various failure mechanisms in the FPZ is the same before the peak, at the peak, and after the peak.
7. Finally, it should be emphasized that numerical models that assume a constant fracture energy or a negligible FPZ width such as LEFM and CCM cannot capture the effects of crack-parallel compression on the fracture behavior of quasi-brittle materials. Yet these effects are ubiquitous in practical design problems (as described in Zhang and Bažant (2023)).

CRediT authorship contribution statement

Yuhui Lyu: Conceptualization, Data curation, Formal analysis, Investigation, Methodology, Software, Validation, Visualization, Writing – original draft. **Madura Pathirage:** Conceptualization, Data curation, Formal analysis, Investigation, Methodology, Validation, Supervision, Writing – review & editing. **Hoang T. Nguyen:** Conceptualization, Methodology. **Zdeněk P. Bažant:** Conceptualization, Formal analysis, Methodology, Writing – review & editing, Funding acquisition, Project administration, Resources, Supervision. **Gianluca Cusatis:** Conceptualization, Formal analysis, Investigation, Methodology, Writing – review & editing, Project administration, Resources, Supervision.

Declaration of competing interest

The authors declare that they have no known competing financial interests or personal relationships that could have appeared to influence the work reported in this paper.

Data availability

Data will be made available on request.

Acknowledgments

Partial financial support under National Science Foundation (NSF) grant CMMI-202964 and ARO grant W911NF-19-1-003, both to Northwestern University, is gratefully acknowledged.

References

Alnaggar, M., Cusatis, G., Luzio, G.D., 2013. Lattice discrete particle modeling (LDPM) of Alkali Silica reaction (ASR) deterioration of concrete structures. Cem. Concr. Compos. 41, 45–59.

Angiolilli, M., Gregori, A., Pathirage, M., Cusatis, G., 2020. Fiber Reinforced Cementitious Matrix (FRCM) for strengthening historical stone masonry structures: Experiments and computations. Eng. Struct. 224, 111102.

Angiolilli, M., Pathirage, M., Gregori, A., Cusatis, G., 2021. Lattice discrete particle model for the simulation of irregular stone masonry. J. Struct. Eng. 147 (9), 04021123.

Barenblatt, G.I., 1959. The formation of equilibrium cracks during brittle fracture. General ideas and hypotheses. Axially-symmetric cracks. J. Appl. Math. Mech. 23 (3), 622–636.

Bažant, Z.P., 1976. Instability, ductility, and size effect in strain-softening concrete. J. Eng. Mech. Div. 102 (2), 331–344.

Bažant, Z.P., 1984. Size effect in blunt fracture: concrete, rock, metal. J. Eng. Mech. 110 (4), 518–535.

Bažant, Z.P., 1990. Justification and improvement of Kienzler and Herrmann's estimate of stress intensity factors of cracked beam. Eng. Fract. Mech. 36 (3), 523–525.

Bažant, Z.P., 1999. Size effect on structural strength: a review. Arch. Appl. Mech. 69 (9), 703–725.

Bažant, Z.P., 2002a. Scaling of Structural Strength. CRC Press.

Bažant, Z.P., 2002b. Concrete fracture models: testing and practice. Eng. Fract. Mech. 69 (2), 165–205.

Bažant, Z.P., Caner, F.C., Carol, I., Adley, M.D., Akers, S.A., 2000. Microplane model M4 for concrete. I: Formulation with work-conjugate deviatoric stress. J. Eng. Mech. 126 (9), 944–953.

Bažant, Z.P., Cedolin, L., 1979. Blunt crack band propagation in finite element analysis. J. Eng. Mech. Div. 105 (2), 297–315.

Bažant, Z., Cedolin, L., 1991. Stability of structures: Elastic, inelastic, fracture and damage theories, 2010.

Bažant, Z., Dönmez, A., Nguyen, H., 2022a. How gap tests of ductile and quasibrittle fracture limit applicability of phase-field, XFEM, cohesive, nonlocal and crack-band models? In: Computational Modelling of Concrete and Concrete Structures. CRC Press, pp. 409–413.

Bažant, Z.P., Dönmez, A.A., Nguyen, H.T., 2022b. Précis of gap test results requiring reappraisal of line crack and phase-field models of fracture mechanics. Eng. Struct. 250, 113285.

Bažant, Z.P., Kazemi, M.T., 1990. Size effect in fracture of ceramics and its use to determine fracture energy and effective process zone length. J. Am. Ceram. Soc. 73 (7), 1841–1853.

Bažant, Z.P., Kazemi, M.T., 1991. Size dependence of concrete fracture energy determined by RILEM work-of-fracture method. Int. J. Fract. 51, 121–138.

Bažant, Z.P., Le, J.-L., Salviato, M., 2021. Quasibrittle Fracture Mechanics and Size Effect: A First Course. Oxford University Press.

Bažant, Z.P., Nguyen, H.T., Dönmez, A.A., 2022c. Scaling in size, time and risk—The problem of huge extrapolations and remedy by asymptotic matching. J. Mech. Phys. Solids 105094.

Bažant, Z.P., Oh, B.H., 1983. Crack band theory for fracture of concrete. Matér. Constr. 16, 155–177.

Bazant, Z.P., Planas, J., 2019. Fracture and Size Effect in Concrete and Other Quasibrittle Materials. Routledge.

Bažant, Z.P., Planas, J., 2019. Fracture and Size Effect in Concrete and Other Quasibrittle Materials. Routledge.

Bazoant, Z., Kim, J., Pfeiffer, P., 1986. Nonlinear fracture properties from size effect tests. J. Struct. Eng. 112 (2), 289–307.

Brockmann, J., Salviato, M., 2022. The gap test: Effects of crack parallel compression on fracture in carbon fiber composites. arXiv preprint arXiv:2207.12649.

Cedolin, L., Cusatis, G., 2007. Cohesive fracture and size effect in concrete. In: Proceedings of the 6th Int Conf on Fracture Mechanics of Concrete and Concrete Structures. Taylor and Francis, London.

Cibelli, A., Pathirage, M., Cusatis, G., Ferrara, L., Di Luzio, G., 2022. A discrete numerical model for the effects of crack healing on the behaviour of ordinary plain concrete: Implementation, calibration, and validation. Eng. Fract. Mech. 263, 108266.

Clough, R.W., 1960. The finite element in plane stress analysis. In: Proc. 2nd ASCE Confer. on Electric Computation, 1960.

Clough, R.W., 1962. The Stress Distribution of Norfork Dam. Technical Report, California Univ Berkeley Inst Of Engineering Research.

Clough, R.W., Wilson, E.L., 1962. Stress Analysis of a Gravity Dam By the Finite Element Method. Laboratório Nacional de Engenharia Civil.

Cusatis, G., 2001. Tridimensional Random Particle Model for Concrete (Civil Engineering Ph.D. thesis). DIS-Politecnico di Milano, Milan, Italy.

Cusatis, G., Bažant, Z.P., Cedolin, L., 2003a. Confinement-shear lattice model for concrete damage in tension and compression: I. Theory. J. Eng. Mech. 129 (12), 1439–1448.

Cusatis, G., Bažant, Z.P., Cedolin, L., 2003b. Confinement-shear lattice model for concrete damage in tension and compression: II. Computation and validation. J. Eng. Mech. 129 (12), 1449–1458.

Cusatis, G., Cedolin, L., 2007. Two-scale study of concrete fracturing behavior. Eng. Fract. Mech. 74 (1–2), 3–17.

Cusatis, G., Mencarelli, A., Pelessone, D., Baylot, J., 2011a. Lattice discrete particle model (LDPM) for failure behavior of concrete. II: Calibration and validation. Cement Concr. Compos. 33 (9), 891–905.

Cusatis, G., Pelessone, D., Mencarelli, A., 2011b. Lattice discrete particle model (LDPM) for failure behavior of concrete. I: Theory. Cem. Concr. Compos. 33 (9), 881–890.

Cusatis, G., Schauffert, E.A., 2009. Cohesive crack analysis of size effect. Eng. Fract. Mech. 76 (14), 2163–2173.

Cusatis, G., Zhou, X., 2014. High-order microplane theory for quasi-brittle materials with multiple characteristic lengths. J. Eng. Mech. 140 (7), 04014046.

Di Luzio, G., et al., 2004. Over-nonlocal microplane model M4: Mode I fracture simulations. In: The Proceedings of the Fifth International Conference on Fracture Mechanics of Concrete and Concrete Structures–FraMCoS-5. p. 287.

Feng, J., Sun, W., Chen, L., Chen, B., Arkin, E., Du, L., Pathirage, M., 2022. Engineered Cementitious Composites using Chinese local ingredients: Material preparation and numerical investigation. Case Stud. Constr. Mater. 16, e00852.

Gettu, R., Saldívar, H., Kazemi, M.T., 1998. Implications of the size effect method for analyzing the fracture of concrete. Int. J. Solids Struct. 35 (31–32), 4121–4132.

Grassl, P., Xenos, D., Nyström, U., Rempling, R., Gylltoft, K., 2013. CDPM2: A damage-plasticity approach to modelling the failure of concrete. International Journal of Solids and Structures 50 (24), 3805–3816.

Green, S., Swanson, S., 1973. Static Constitutive Relations for Concrete. Technical Report, Terra Tek Inc Salt Lake City Ut.

Han, L., Pathirage, M., Akono, A.-T., Cusatis, G., 2020. Lattice discrete particle modeling of size effect in slab scratch tests. J. Appl. Mech. 88 (2).

Hang, S., 2015. TetGen, a Delaunay-based quality tetrahedral mesh generator. ACM Trans. Math. Software 41 (2), 11.

Herrmann, G., Sosa, H., 1986. On bars with cracks. Eng. Fract. Mech. 24 (6), 889–894.

Hillerborg, A., 1983. Analysis of one single crack in fracture mechanics of concrete, edited by FH wittmann.

Hillerborg, A., Modéer, M., Petersson, P.-E., 1976. Analysis of crack formation and crack growth in concrete by means of fracture mechanics and finite elements. Cement. Concr. Res. 6 (6), 773–781.

Huynh, H.D., Nguyen, M.N., Cusatis, G., Tanaka, S., Bui, T.Q., 2019. A polygonal XFEM with new numerical integration for linear elastic fracture mechanics. Eng. Fract. Mech. 213, 241–263.

Ince, R., 2010. Determination of concrete fracture parameters based on two-parameter and size effect models using split-tension cubes. Eng. Fract. Mech. 77 (12), 2233–2250.

Jirásek, M., 2011. Damage and Smeared Crack Models. Springer.

Kienzler, R., Herrmann, G., 1986. An elementary theory of defective beams. Acta Mech. 62 (1–4), 37–46.
Lale, E., Zhou, X., Cusatis, G., 2017. Isogeometric implementation of high-order microplane model for the simulation of high-order elasticity, softening, and localization. J. Appl. Mech. 84 (1).
Li, W., Rezakhani, R., Jin, C., Zhou, X., Cusatis, G., 2017. A multiscale framework for the simulation of the anisotropic mechanical behavior of shale. Int. J. Numer. Anal. Methods Geomech. 41 (14), 1494–1522.
Lyu, Y., Pathirage, M., Ramyar, E., Liu, W.K., Cusatis, G., 2023. Machine learning meta-models for fast parameter identification of the lattice discrete particle model. Comput. Mech. 1–20.
Manual, A.S.U., 2012. Abaqus 6.11, 89, v6, http://130.149.
Mercuri, M., Pathirage, M., Gregori, A., Cusatis, G., 2020. Computational modeling of the out-of-plane behavior of unreinforced irregular masonry. Eng. Struct. 223, 111181.
Mercuri, M., Pathirage, M., Gregori, A., Cusatis, G., 2021. On the collapse of the masonry Medici tower: An integrated discrete-analytical approach. Eng. Struct. 246, 113046.
Mercuri, M., Pathirage, M., Gregori, A., Cusatis, G., 2022. Masonry vaulted structures under spreading supports: Analyses of fracturing behavior and size effect. J. Build. Eng. 45, 103396.
Mercuri, M., Pathirage, M., Gregori, A., Cusatis, G., 2023. Influence of self-weight on size effect of quasi-brittle materials: generalized analytical formulation and application to the failure of irregular masonry arches. Int. J. Fract. 1–28.
Ngo, D., Scordelis, A.C., 1967. Finite element analysis of reinforced concrete beams. In: Journal Proceedings, Vol. 64. pp. 152–163.
Nguyen, H.T., Dönmez, A.A., Bažant, Z.P., 2021. Structural strength scaling law for fracture of plastic-hardening metals and testing of fracture properties. Extreme Mech. Lett. 43, 101141.
Nguyen, H.T., Pathirage, M., Cusatis, G., Bažant, Z.P., 2020a. Gap test of crack-parallel stress effect on quasibrittle fracture and its consequences. J. Appl. Mech. 87 (7), 071012.
Nguyen, H., Pathirage, M., Rezaei, M., Issa, M., Cusatis, G., Bažant, Z.P., 2020b. New perspective of fracture mechanics inspired by gap test with crack-parallel compression. Proc. Natl. Acad. Sci. 117 (25), 14015–14020.
Ožbolt, M.P.J., 1996. Smeared crack approaches-material modeling. J. Eng. Mech. 545.
Pathirage, M., Bentz, D., Di Luzio, G., Masoero, E., Cusatis, G., 2019a. The ONIX model: a parameter-free multiscale framework for the prediction of self-desiccation in concrete. Cem. Concr. Compos. 103, 36–48.
Pathirage, M., Bousikhane, F., D'Ambrosia, M., Alnaggar, M., Cusatis, G., 2019b. Effect of alkali silica reaction on the mechanical properties of aging mortar bars: Experiments and numerical modeling. Int. J. Damage Mech. 28 (2), 291–322.
Pathirage, M., Tong, D., Thierry, F., Cusatis, G., Grégoire, D., Pijaudier-Cabot, G., 2023a. Discrete modeling of concrete failure and size-effect. Theor. Appl. Fract. Mech. 124, 103738.
Pathirage, M., Zhang, B., Alnaggar, M., Cusatis, G., 2023b. Confinement and alkali-silica reaction in concrete: Review and numerical investigation. Int. J. Solids Struct. 112341.
Pijaudier-Cabot, G., Toussaint, D., Pathirage, M., Grégoire, D., Vermorel, R., Cusatis, G., 2022. Surface and size effects on elasticity and fracture. In: Computational Modelling of Concrete and Concrete Structures. CRC Press, pp. 46–55.
Rashid, Y.R., 1968. Ultimate strength analysis of prestressed concrete pressure vessels. Nucl. Eng. Des. 7 (4), 334–344.
Rezakhani, R., Scott, D.A., Bousikhane, F., Pathirage, M., Moser, R.D., Green, B.H., Cusatis, G., 2021. Influence of steel fiber size, shape, and strength on the quasi-static properties of ultra-high performance concrete: Experimental investigation and numerical modeling. Constr. Build. Mater. 296, 123532.
Scanlon, A., 1971. Time dependent deflections of reinforced concrete slabs.
Schauffert, E.A., Cusatis, G., 2011. Lattice discrete particle model for fiber-reinforced concrete. I: Theory. J. Eng. Mech. 138 (7), 826–833.
Schlangen, E., Van Mier, J., 1992. Micromechanical analysis of fracture of concrete. Int. J. Damage Mech. 1 (4), 435–454.
Shah, S.P., 1990. Size-effect method for determining fracture energy and process zone size of concrete. Mater. Struct. 23, 461–465.
Tschegg, E., Elser, M., Stanzl-Tschegg, S., 1995. Biaxial fracture tests on concrete—development and experience. Cem. Concr. Compos. 17 (1), 57–75.
Yang, L., Pathirage, M., Su, H., Alnaggar, M., Di Luzio, G., Cusatis, G., 2021. Computational modeling of temperature and relative humidity effects on concrete expansion due to alkali–silica reaction. Cem. Concr. Compos. 124, 104237.
Yang, L., Pathirage, M., Su, H., Alnaggar, M., Di Luzio, G., Cusatis, G., 2022. Computational modeling of expansion and deterioration due to alkali–silica reaction: Effects of size range, size distribution, and content of reactive aggregate. Int. J. Solids Struct. 234–235, 111220.
Zhang, Y., Bažant, Z.P., 2023. Smooth Crack Band model—A computational paragon based on unorthodox continuum homogenization. J. Appl. Mech. 90 (4), 041007.
Zhu, Z., Pathirage, M., Wang, W., Troemner, M., Cusatis, G., 2022. Lattice discrete particle modeling of concrete under cyclic tension–compression with multi-axial confinement. Constr. Build. Mater. 352, 128985.
Zubelewicz, A., Bažant, Z.P., 1987. Interface element modeling of fracture in aggregate composites. J. Eng. Mech. 113 (11), 1619–1630.